‘

Experimental and theoretical investigation of the crystalline surface, film, and interface properties of antiperovskite Mn_3GaN grown by molecular beam epitaxy on MgO(001)

Ali Abbas[1], Juan Carlos Moreno Hernandez[5], Ashok Shrestha[1],
Daniel Russell[3], Tyler Erickson[1], Kai Sun[2], Gregorio
Hernandez Cocoletzi[4], Fengyuan Yang[3] and Arthur R. Smith[1,a]
[1]*Nanoscale and Quantum Phenomena Institute,*
Department of Physics and Astronomy,
Ohio University, Athens, OH 45701, USA

[2]*Michigan Center for Materials Characterization (MCMC)*
Department of Materials Science and Engineering,
The University of Michigan Ann Arbor, MI 48109, USA

[3]*Department of Physics,*
The Ohio State University,
191 Woodruff Avenue,
Columbus, OH 43210, USA

[4]*Universidad Autónoma de Puebla,*
Instituto de Física, Apartado Postal J-48,
Puebla 72570, México
and
[5]*Centro de Servicio de Alta Tecnología,*
Universidad Popular Autónoma del Estado de Puebla,
Puebla 72410, México

---

[a] Corresponding Author : smitha2@ohio.edu

(Dated: June 3, 2025)

Abstract

We present a study of the epitaxial growth, characterization, and theoretical modeling of thin film antiperovskite Mn_3GaN, an antiferromagnetic material with kagome structure which is grown on MgO (001) substrates using N-plasma-assisted molecular beam epitaxy. Reflection high energy electron diffraction is used to assess the *in-plane* evolution of the film structure during growth, and the surface is investigated *in-situ* using scanning tunneling microscopy and Auger electron spectroscopy. These results are combined with precision measurements done *ex-situ* determining the film lattice constants using a combination of x-ray diffraction with reciprocal space mapping and scanning transmission electron microscopy. Overall, a uniform, homogeneous film with an atomically smooth vacuum surface and atomically sharp substrate interface is found having very small *in-plane* tensile strain and mild *out-of-plane* compressive strain. First-principles theoretical calculations are applied in order to ascertain the lowest energy models for both the Mn_3GaN surface and the Mn_3GaN/MgO film/substrate interface. Models including MnGa versus MnN surface layers and MnGa versus MnN interfacial layers are considered as functions of both the Mn and Ga chemical potentials. The predictions are discussed in comparison to the experimental results. The overall findings suggest that Mn_3GaN on MgO(001) is a viable epitaxial film which can be further explored in connection with antiferromagnetic spintronics.

I. INTRODUCTION

Antiferromagnetic (AFM) materials having non-collinear structures exhibit interesting properties due to their spin configurations. Hexagonal antiferromagnetic compounds like Mn_3Sn [1][2] and Mn_3Ga [3][4] are currently of very high interest. At the same time, these same compounds, when combined with nitrogen, form interesting kagome spin materials having cubic, rather than hexagonal, crystal structures. These are known as antiperovskites, space group Pm3m no. 221. Among the broader antiperovskite family, Mn-based antiperovskites are a magnetic sub-class having the general formula Mn_3YZ, where Y could be Ga, Zn, Ag, Sn, or some other metallic element. Element Z is a non-metallic element such as C, N, or O which, in the antiperovskite structure, resides at the body center, as compared to the perovskite family in which the non-metallic element usually resides at the face centers [5, 6]. These multifunctional antiperovskite materials exhibit kagome spin structures and magnetic phase transitions. They have been studied for the past few decades using neutron diffraction [5], nuclear magnetic resonance [7], and magnetic susceptibility [8] [9]. Of the general class of Mn-based antiperovskites, the Mn antiperovskite nitride family, including Mn_3GaN, Mn_3ZnN, Mn_3AgN, and Mn_3SnN, is currently gaining a lot of interest. One reason is the possibility of combining kagome antiferromagnetic materials with wide band gap semiconductors for spintronic applications.

Mn_3GaN has attracted recent interest due to a variety of physical properties, including antiferromagnetism [10], giant barocaloric effect [11], superconductivity [12] and giant magnetoresistance [13]. The Mn spins form a triangular Γ5g kagome-like spin structure, as shown in Fig. 1(a)(b), depicting frustrated antiferromagnetic spin coupling in the kagome lattice plane. In the bulk, Mn_3GaN is known to exhibit antiferromagnetic ordering with a non-collinear spin structure in the (111) plane. Thus, it leads to the formation of non-collinear antiferromagnetic (NCAF) spin textures. Below the Neel temperature ($T_N = 298K$), this 120° triangular chiral configuration exhibits an anomalous Hall conductivity (AHC) in the (111) Kagome plane[14].

Kim *et al.* studied the molecular beam epitaxial (MBE) growth of GaN and diluted $Ga_{1-x}Mn_xN$ using a single Ga precursor with an Mn solid source. In their experiments, GaN and dilute GaMnN layers were grown on sapphire (0001) and GaAs (001) substrates at various temperatures ranging from 500°C to 800°C. Alongside the main layer growth, they observed cubic Mn_3GaN as a precipitate [15][16]. Not long after this, Lukashev *et al.* predicted that the magnetic structure of Mn_3GaN could be controlled by applying bi-axial strain[17]. Sunao *et al.* studied the Mn_3GaN_{1-x} thin films using magnetron sputtering and showed that the deposition rate and the N_2 gas partial pressure could control the tetragonal distortion of the films[18]. More recently, and seemingly consistent with Lukashev *et al.*, Nan *et al.* reported non-zero unconventional spin torque in a 30-nm Mn_3GaN film grown by DC reactive magnetron sputtering on $LaSrAlTaO_3$ and inferred that it was due to a tetragonal distortion inducing a small, non-compensated magnetic moment[19]. Recently, Rimmler *et al.* reported the growth of Mn_3SnN and Mn_3GaN (25-nm) films by RF-plasma MBE on (001)-oriented MgO substrates, observing the spin Hall effect but attributing it to manganese atomic displacements rather than tetragonal distortion alone[20].

Due to great interest in the spintronic effects of Mn_3GaN and similar materials (Mn_3SnN for example), it is important to fully characterize the film lattice parameters, including *in-plane* and *out-of-plane* strains, and the chemical compositions for MBE-grown thin films. Since the origins of important observed effects such as spin Hall effect and anomalous Hall effect are in question, careful characterization studies such as shown here are critical for achieving better understanding in these materials. In this paper, we experimentally explore the detailed structural and chemical properties of Mn_3GaN films grown by MBE on (001)-oriented MgO substrates and, in addition, we theoretically investigate the substrate and vacuum interface configurations in the case of Mn_3GaN in order to gain a better understanding of the interfacial bonding and surface structure.

II. EXPERIMENTAL AND THEORETICAL METHODS

A. Experimental

Thin films of Mn_3GaN were deposited on a titanium back-coated MgO (001) substrate using a custom-built MBE system with ultra-high vacuum (UHV) chambers with base pressures of 1.0×10^{-9} Torr and equipped with an N_2 radio frequency (RF) plasma source, Mn and Ga effusion cells, and a quartz crystal sensor for source flux calibration. A STAIB Instruments reflection high-energy electron diffraction (RHEED) system monitors the epitaxial development during crystal formation with a 20 keV incident electron beam. The MgO (001) substrate was cleaned with acetone and isopropanol before loading into the chamber. The substrate was annealed at 1000 ± 50°C for an hour in a 2.0×10^{-5} Torr N_2 plasma until the RHEED pattern was streaky along both [100] and [110] directions of the MgO.

To achieve a close to 3:1:1 ratio of Mn:Ga:N, the Mn and Ga flux ratio used was 3.11 ± 0.10. Fluxes were measured by a quartz crystal thickness monitor (QCM). MBE growth was carried out using Mn and Ga fluxes of $\sim 8.70 \times 10^{14}$ atoms/cm^{2}s and $\sim 2.80 \times 10^{14}$ atoms/cm^{2}s, respectively. The RF plasma nitrogen source was operated to give a flux of $\sim 3.50 \times 10^{14}$ atoms/cm^{2}s as determined by the Ga-rich/N-rich crossover point in GaN growth. Given the flux ratios used, we have N-rich growth since, when normalized to N flux ($F_N = 1.00$), Mn and Ga are 2.49 (< 3) and 0.80 (< 1), respectively. The growth stage temperature was ramped down to $T_S = 250$°C to grow the Mn_3GaN samples. The Mn and Ga shutters were subsequently opened to allow Mn_3GaN sample growth to begin, with a growth rate of 10 nm/min.

The reconstructed sample surface is continuously monitored throughout the growth using RHEED. The growth was terminated by closing the Mn and Ga shutters simultaneously and switching off the RF plasma source after 25 min of growth, resulting in a 250 nm thin film, and then slowly ramping down the growth stage temperature using a PID controller. Following the growth process, the sample was transferred *in-situ* to the surface analysis chamber, maintaining vacuum integrity, and allowed to cool to room temperature. The surface analysis chamber has a room-temperature scanning tunneling microscope (RT-STM) system and an Auger electron spectroscopy (AES) system. RT-STM imaging utilized RHK's SPM 100 system in constant-current mode, employing an electrochemically etched tungsten tip for scanning. The surface chemistry of the grown sample was studied by *in-situ* Auger electron spectroscopy (AES).

After removing the sample from the vacuum, *ex-situ* analysis using Bragg-Brentano θ-2θ X-ray diffraction (XRD) was performed using a Rigaku MiniFlex XRD system with a Cu Kα X-ray source of wavelength 1.541 Å. Scanning transmission electron microscopy (STEM) and Energy-dispersive x-ray spectroscopy (EDS) were performed in the Michigan Center for Materials Characterization (MCMC) at the University of Michigan. An *in-situ* FIB lift-out process was utilized for sample preparation, conducted using a Thermo-Fisher Xe plasma G4 dual-beam focused ion beam (FIB) system, optimizing beam parameters to 5 keV and 10 pA. Elemental mapping utilized a Thermo-Fisher Talos F200 TEM with four 30 mm^2 SSD X-ray detectors, operating in both STEM and TEM modes. High-resolution imaging employed a JEOL JEM-3100R05 microscope with double aberration correction, and simultaneous high-angle annular dark-field (HAADF) and bright-field (BF) imaging were performed in STEM mode.

B. Theoretical

Non-collinear *ab-initio* calculations were performed using the Vienna Ab-initio Simulation Package (VASP) software [21]. The interactions between core ions and valence electrons were treated within the PAW pseudopotentials scheme [22]. The generalized gradient approximation in the Perdew-Burke-Ernzerhof format scheme (GGA-PBE) [23] was applied to describe the exchange-correlation energy. The cutoff radius for the kinetic energy was set to 520 eV. The supercell method was used to model the different interfaces with a space of 15 Å along the Z direction. The interfaces employed six atomic layers for MgO (001) and Mn_3GaN (001) surfaces. Because we employed non-collinear calculations, the spin-orbit coupling breaks the structural symmetries of the MgO (001) surface. The forces on the ions were less than 0.001 eV/Å, and the total energy was converged to 10^{-6} with the Gaussian smearing method. The inversion symmetry was not used in the models. The first Brillouin zone was described by k-point Monkhorst-Pack mesh [24] of $7 \times 7 \times 1$. The calculated MgO lattice constant in bulk was 4.25 Å, which agrees with experimental and theoretical data [25, 26]. We obtained an a value of 3.85 Å for Mn_3GaN in bulk, leading to an average error of less than 1.5% compared with experimental results[5].

III. RESULTS AND DISCUSSION

A. Growth and Surface Analysis by RHEED

1. *RHEED Patterns during and after MBE Growth*

The evolution of the RHEED patterns during sample growth is shown in Fig. 2. It has eight panels (a-h). The left panel indicates the $[100]_{MgO}$ and the right panel indicates the $[110]_{MgO}$ direction. Fig. 2(a-b) shows the bright streaks along with sharp Kikuchi lines in [100] and [110] directions of the MgO (001) substrate after 1 h of annealing at

1000°C. After opening the shutter, the growth starts and Fig. 2(c-d) shows the RHEED pattern after 25 minutes of growth, while still at the growth temperature of 250 °C. The RHEED pattern looks clear and streaky, but not so sharp, in the zeroth-order Laue rings. Both 1st order and 1/2 order streaks are seen. The broad-width streaks at the growth temperature suggest a certain amount of atomic movement at the surface, with a relatively small coherence length[27]. The sample was cooled down to room temperature, and the RT RHEED patterns appear sharper as shown in Fig. 2(e-f) at the 60 min point (since the start of growth). The sample was maintained at RT until the next day, and the RHEED patterns shown in Figs. 2(g-h) appear very streaky with half-order streaks along [100] appearing clearly.

The appearance of sharp half-order streaks, suggesting a 2×1 surface periodicity, was continuously observed. This can be explained by the structure of Mn_3GaN, in which for the (001) MnGa plane, a Mn atom resides at the face center, with Ga atoms at the corners of the conventional unit cell, creating a real-space periodicity doubling for [100] (but not for [010]). It can also be explained from the perspective of the (001) Mn_2N plane in a similar way. Note there is no 1/2-order streak for MgO because of its 1:1 stoichiometry and because the face center atom and corner atoms in any (001) plane are all the same. Similar half-order streaks as for Mn_3GaN were seen by Foley *et al.* and Shrestha *et al.* while growing cubic ϵ-phase Mn_4N [28] and ζ-phase Mn_2N[29].

2. *Line Profile Analysis of RHEED images*

The RHEED line profiles including 1st-order and 1/2-order streaks can be seen in Fig. 3. The *in-plane* lattice spacings along $[100]_{Mn_3GaN}$ and $[110]_{Mn_3GaN}$ directions are determined using line profiles. Line profiles of the MgO substrate along $[100]_{MgO}$ and $[110]_{MgO}$ are shown in Fig. 3(a-b). Line profiles for the Mn_3GaN surfaces along $[100]_{MGN}$ and $[110]_{MGN}$ are shown in Fig. 3(c-h). The less bright and broader-streak line profiles evident in Figs. 3(c-d) indicate mobile atom species and/or smaller coherence domain sizes at 250 °C. After cooling down to room-temperature (at the 60-minute mark), 1st-order and 1/2-order peaks become sharper which indicates that the surface lattice periodicity is becoming more coherent. It indicates a more well-ordered surface. Since the film streak symmetries follow from the substrate streak symmetries, we can infer that that the Mn_3GaN film grows epitaxially on MgO (001) with (001) film orientation and crystallograhic orientation relationship is $[100]_{MGN} \parallel [100]_{MgO}$ and $[110]_{MGN} \parallel [110]_{MgO}$, despite an expected lattice mismatch δ of -7.48% defined as $\delta = \frac{a_{Mn_3GaN} - a_{MgO}}{a_{MgO}}$ and where the bulk values used are $a_{MGN} = 3.898$ Å and $a_{MgO} = 4.213$ Å).[5]

Lattice constants are determined from the $[100]_{MGN}$ and $[110]_{MGN}$ line profiles using Lorentzian peak fitting of the 1st-order streaks in order to precisely determine the spacings between peak centroids of the (-1,0) and (+1,0) peaks. Lorentzian peak fitting was also applied to the MgO patterns, also along both [100] and [110], in order to calibrate the RHEED patterns accurately. This method results in highly precise lattice parameters, with relative errors of ± 0.03 % or better for a given line profile. However, more variation was found among different line profiles, and so to take into account profile-to-profile random variations, we took straight averages and standard deviations for the two RT [100] line profiles and for the two RT [110] line profiles separately [see Figs. 3(e,f) and (g,h)], and we find $a_{MGN,[100]} = 3.958 \pm 0.005$ Å along [100] and $a_{MGN,[110]} = 3.936 \pm 0.017$ Å along [110]. The average lattice constant among all 4 line profiles [from patterns (e), (f), (g), and (h)] along both [100] and [110] was also taken as a straight average from all these individual values with their standard deviation and found to be 3.947 ± 0.017 Å. These values can be compared to the bulk value (3.898 Å) reported by Bertaut *et al.*[5]

3. Evaluation of RHEED Streak Widths

The coherence length (or 'domain width') L_c of the surface is inversely related to the half-width Γ of the RHEED streaks via the relation: $L_c = 2\pi/(\Gamma cos(\theta))$, where Γ is in units of inverse Å and θ is the diffraction angle, as discussed by Van Hove *et al.*[30]. Note the Van Hove formula is essentially equivalent to the Scherrer equation if the wave vector k is extracted out of Γ leaving the familiar $D = K\lambda/Bcos(\theta)$, K being the Scherrer constant $\sim$ 0.9, λ being the wavelength, and B being the streak angular width in radians. By analyzing the half-widths of the RHEED streaks, we can determine how L_c evolved over the time of the sample growth. To do this, for each primary peak of the RHEED patterns shown in Fig. 3, a straight line (local) background was subtracted, and Γ' was then measured, where Γ' is related to Γ by $\Gamma = \Gamma' - \Delta_{Instr}$ and where Δ_{Instr} is the instrumental broadening. We took an average of the measured Γ''s from the +1 and -1 streaks for each pattern, and a plot showing the progression of the average Γ' over the growth time t was then created, as shown in Fig. 3(i).

There we can see that the (uncorrected) half-width Γ' began at a total value of 0.35/Å for [100] (0.32 /Å for [110]). After just 25 min of growth, Γ' increased to 0.58/Å ([100] and [110]), corresponding to a decrease in coherence length in the early stage of growth. After 60 min, Γ' reduced to 0.35/Å for [100] (0.43/Å for [110]), indicating an increased surface coherence length. Finally, Γ' came to 0.41/Å for [100] (0.39/Å for [110]) by the next day. (Note: it is unknown why Γ' for [100] at the 60 min point (35 min after stopping the growth) is slightly smaller than the Γ' value after one day).

In order to determine an approximate value for the instrumental broadening, we grew a highly smooth GaN(000$\bar{1}$) surface in our MBE chamber and extracted an average streak width from the [11$\bar{2}$0] RHEED pattern (1st order streaks), obtaining a value of 0.235 /Å. This will be an upper limit for Δ_{Instr}. Subtracting this value from the 0.40 /Å for the Mn_3GaN, we get a value for Γ = 0.165 /Å, corresponding to a value for L_c (or *in-plane* domain width) of 38 Å. This value, although not large, is comparable to about half a terrace width (see STM image section).

B. Crystallinity by X-ray Diffraction

1. *Determination of Lattice Spacing*

To understand the crystallinity and orientation of Mn_3GaN thin film, XRD measurements were taken with a Cu Kα X-ray source containing both $K_{\alpha1}$ and $K_{\alpha2}$ X-rays. Figure 4 shows the XRD spectra for the Mn_3GaN sample as intensity (log scale) vs. 2θ (°). We observe two major peaks and two minor peaks, including a minor 001 peak at 23.08° and a major 002 peak at 46.87°, both of Mn_3GaN, with relative intensities of 0.5% and 77.8% of the MgO 002 peak, respectively. Finally, a minor peak of Mn_3GaN 111 is seen at 38.57° corresponding to a d-spacing of 4.669 ± 0.011 Å. The major MgO 002 peak is observed at 42.94°, giving a perpendicular d spacing of 2.106 ± 0.004 Å corresponding to $c = 2d = 4.213$ Å, in good agreement with the expected lattice constant of MgO[31][32] at 300K.

The determined lattice constant LC values from the 001 and 002 XRD peaks of the Mn_3GaN film are 3.855 ± 0.014 Å and 3.878 ± 0.008 Å. The weighted average LC value is 3.872 ± 0.007 Å. Due to the accommodation of lattice mismatch (-7.48%), we can see *out-of-plane* compressive strain of -1.10 % from the 001 peak and -0.51 % from the 002 peak. A summary of the XRD results is given in Table. I.

Non-uniform strain over the film thickness leads to broadening of the Mn_3GaN 002 peak with a full-width half maxima (FWHM) of 0.66 ± 0.10°, as shown in the zoomed-in inset view of 002 MgO and 002 Mn_3GaN. We can apply Scherrer's equation[33, 34] to determine the *out-of-plane* crystallite domain size. Scherrer's equation is:

$$D_{hkl} = \frac{K\lambda}{B_{hkl} cos\theta} \tag{1}$$

and taking the crystallite-shape factor $K = 0.9$, the XRD wavelength $\lambda = 1.542$ Å, the 002 peak's angular half-width $B_{002} = \frac{1.08^\circ}{2}(\frac{\pi}{180^\circ}) = 0.005759$ rad, and $\theta = 23.435^\circ$, we get D_{002} = 263 Å.

2. *Reciprocal Lattice Mapping at Off-Axis Angle*

The reciprocal spatial map (RSM) around the MgO asymmetric 113 spot plotted in $Q_x - Q_z$ space is illustrated in Fig. 4(b). Both the MgO and the Mn_3GaN elliptical spot are clearly distinguished. The *in-plane* and *out-of-plane* lattice parameters are calculated after precise calibration to the MgO spot in both the x and z directions. The lattice parameters for Mn_3GaN can be determined using equations $Q_x = \frac{\sqrt{h^2+k^2}}{a}$ and $Q_z = \frac{l}{a}$. The *in-plane* lattice constant, a_{Mn_3GaN} was measured to be 3.850 ± 0.051 Å. Conversely, the *out-of-plane* lattice constant, c_{Mn_3GaN}, was found to be 3.880 ± 0.008 Å. The *out-of-plane* -0.46 % (compressive) strain is consistent with the 001 and 002 peak values derived from XRD. Remarkably, the *in-plane* lattice constant from RSM, when compared to the reported 3.898 Å bulk value, corresponds to 1.23 % strain, also compressive; however, the large error bar means that it does not greatly affect the lattice constant weighted averages from our measurements as discussed in the below section.

The ideal angle η (for a perfectly cubic structure) shown in Fig. 4(b) equals $\tan^{-1}(\Delta Q_x/\Delta Q_z)$ $= \tan^{-1}(\sqrt{2}/3) = 25.24^\circ$, and the measured value for η at midpoint 2 in the figure is 27.40 ± 8.07 °. Therefore, the value is in agreement with the expected, but it has a large width (uncertainty).

TABLE I. Summarized table showing experimental and reported [5][31] d values for different peak positions observed on XRD scan.

2θ (degree)	Peak label	Plane hkl	Experimental d value (Å)	Reported d value (Å)	Relative Intensity A.U.
23.08°	Mn_3GaN	001	3.855 ± 0.014	3.898	0.05
38.57°	Mn_3GaN	111	2.330 ± 0.011	2.250	0.03
42.94°	MgO	002	2.106 ± 0.004	4.213	1.00
46.87°	Mn_3GaN	002	1.939 ± 0.008	1.949	0.78

C. X-Sectional and Lattice imaging from STEM

Atomically resolved bright-field (BF) and high-angle annular dark-field (HAADF) image of Mn_3GaN grown on MgO are shown in Fig. 5(a)(c). Mn_3GaN layer appears to be dark in the BF image and light in the HAADF region. This color contrast is produced by the different charge densities of Mn_3GaN and MgO. The bright-field image captured in Fig. 5(a) provides a detailed depiction of both the substrate and the sample, showcasing a well-defined and organized interface. Noteworthy is the observation of the pseudomorphically strained Mn_3GaN film, matching one-to-one with the MgO substrate lattice at the interface along the yellow dotted line.

Figure. 5(b) shows the elemental composition maps of Mn, Ga, and N. The uniform composition across the film indicates highly uniform and crystalline growth. Upon close examination of the STEM-HAADF image of Mn_3GaN in Fig. 5(c), a distinct pattern emerges, revealing alternating dark and bright spots corresponding to Ga and Mn atoms in one row, followed by a row solely composed of Mn atoms. Fig. 5(d) shows a zoomed-in view of the dashed red square region seen in Fig. 5(c), overlaid with green and magenta atoms on Mn and Ga atomic sites. This observation verifies the cube-on-cube (001)-oriented crystal alignment of the film, as modeled in Fig. 5(e)[36]. As shown in Fig. 5(f), the Mn_3GaN layer is continuous and flat over large distances as indicated by the wide-view STEM image.

We use the HAADF STEM image of the MgO substrate to calibrate the image scale in Fig. 5(c), resulting in a measured value for the *in-plane* spacing of 3.930 ± 0.020 Å, in good agreement with the RHEED value (3.947 ± 0.017Å) and corresponding to a tensile strain of +0.82 % compared to the expected $a = 3.898$ Å[5]. The *out-of-plane* spacing is measured at 3.845 ± 0.020 Å, in good agreement with the weighted average XRD value from 001 and 002 peaks (3.872 ± 0.009 Å) and corresponding to a compressive strain of -1.36 %.

D. Summary of Lattice Constants, *In-plane* and *Out-of-plane* Strains, and Poisson's Ratio

The results for *in-plane* (transverse) and *out-of-plane* (longitudinal) lattice parameters are summarized in Table II and also in a graphical form in the Supplementary file (Fig. S2). Using these experimental values, together with the measurement uncertainties, we derive a value for the inverse-sigma-squared (quadrature method) weighted average for the *in-plane* LC (a_t) of 3.934 ± 0.013 Å, and for the *out-of-plane* LC (a_l) a value of 3.874 ± 0.005 Å).

To determine strain values, we take as a fixed reference point the published theoretical value for Poisson's ratio from the Materials Database, $\mu = 0.260$. We make the assumption that this value is not greatly dependent on small variations of stoichiometry or small variations of lattice constant, and then we use our measured weighted average a_t and a_l values to determine a new experimental value for a_{MGN} using the formula:

$$\mu_{MGN} = -\epsilon_t/\epsilon_l \tag{2}$$

which can be expanded and rearranged to give:

$$a_{MGN} = \frac{a_t + \mu\ a_l}{1 + \mu} \tag{3}$$

The resulting value is $a_{MGN} = 3.922 \pm 0.011$ Å, which is very close to the equilibrium lattice parameter in AFM configuration.[37] This determines the strain values for the film (ϵ_t and ϵ_l), and the measured and derived values are all shown in Table II.

We can also calculate the degree of relaxation δ of the film using the derived a$_{MGN}$ value and the following formula:

$$\delta = \frac{a_{MGN,t} - a_{MgO,t}}{a_{MGN} - a_{MgO,t}} \tag{4}$$

which yields $\delta = 95.9 \pm 8.1$ % relaxed. Note that $\delta = 0\%$ indicates a film fully strained to its substrate, whereas $\delta = 100\%$ indicates a fully relaxed film[35]. Therefore, to one sigma uncertainty, the result is consistent with a fully *in-plane* relaxed film, consistent with $\epsilon_t = 0.31$ %.

TABLE II. Summary table showing *in-plane* and *out-of-plane* lattice constants for *in-situ* and *ex-situ* measurements, the weighted average values, the derived experimental lattice constant for Mn_3GaN, and the derived strain values assuming the theoretical value for Poisson's ratio.

Orientation	RHEED (Å)	RSM (Å)	STEM (Å)	XRD (Å)	Weighted Ave (Å)	Strain (%)
In-plane	3.947 ± 0.017	3.850 ± 0.050	3.930 ± 0.020	-	3.934 ± 0.013	+0.31 ± 0.34
Out-of-plane	-	3.880 ± 0.008	3.845 ± 0.020	3.872 ± 0.007	3.874 ± 0.005	-1.22 ± 0.13

Experimental value for $a_{MGN} = 3.922 \pm 0.011$Å

Theoretical Poisson's ratio = 0.260

E. Elemental Mapping from STEM - Energy Dispersive Spectroscopy

Fig. 6(a) shows the EDS elemental mapping of the film and the substrate including at the interface and also at the surface. EDS line profiles are taken near the interface. The average elemental compositions near the interface (see Supplemental) are measured to be (Mn) 34.8 ± 3.4 atomic %, (Ga) 12.4 ± 2.4 atomic % and (N) 2.0 ± 1.4 atomic %. Shown in Fig. 6(b) are plots of the stoichiometric ratios Mn:Ga, N:Ga and Mg:O as a function of position along the interface in nm. These ratios are depicted with grey, red, and blue color profiles, respectively. The averaged Mn:Ga, N:Ga and Mg:O ratios are calculated to be 2.81 ± 0.79, 0.16 ± 0.14, and 1.21 ± 0.34 respectively. Note the large amount of uncertainty owing to a large amount of fluctuation in the data values from this measurement. Even the Mg:O ratio (1.21 ± 0.34) shows a large fluctuation but easily agrees with a 1:1 Mg:O ratio.

The Mn:Ga ratio (2.79 ± 0.79) average matches 3:1 easily within the fluctuations of the data. This data suggests a very small N:Ga ratio (0.16 ± 0.14), but it is well known that EDS is not very sensitive to N and lighter elements, so this N:Ga value is not reliable.

F. Surface Chemical Composition from AES

1. *Gallium to Manganese and Gallium to Nitrogen Ratios*

The stoichiometry of the upmost surface layers of the sample grown with a Mn:Ga flux ratio of 3.11:1.00 was determined using *in-situ* Auger electron spectroscopy by acquiring AES spectra with an incident electron beam of 5.000 keV. From the AES measurements, the ratios of Mn:Ga and N:Ga are calculated based on the following equations:

$$Mn : Ga = \frac{(I^{pp}_{Mn}/S_{Mn})}{(I^{pp}_{Ga}/S_{Ga})} = (\frac{I^{pp}_{Mn}}{I^{pp}_{Ga}})(\frac{S_{Ga}}{S_{Mn}}) \tag{5}$$

$$N : Ga = \frac{(I^{pp}_{N}/S_{N})}{(I^{pp}_{Ga}/S_{Ga})} = (\frac{I^{pp}_{N}}{I^{pp}_{Ga}})(\frac{S_{Ga}}{S_{N}}) \tag{6}$$

$$N : Mn = \frac{(I^{pp}_{N}/S_{N})}{(I^{pp}_{Mn}/S_{Mn})} = (\frac{I^{pp}_{N}}{I^{pp}_{Mn}})(\frac{S_{Mn}}{S_{N}}) \tag{7}$$

where I^{pp}_{Mn}, I^{pp}_{Ga}, I^{pp}_{N} are the peak-to-peak intensities of the $dN(E)/dE$ versus E curves for Mn, Ga and N, respectively, and where $S_{Mn_{592}}$, $S_{Ga_{1069}}$ and $S_{N_{389}}$ represent the sensitivity factors of Mn, Ga, and N, respectively (measured in our AES system using calibration samples). Fig. 6(c) shows the AES spectra taken at the three different positions of the sample. The results for the averages from three spots on the sample surface are given in Table III.

Here, the measured Mn:Ga ratio is within $\sim$ 4.3% of the ideal 3:1 Mn:Ga ratio (for Mn_3GaN) and only 0.74 % larger than the incident Mn:Ga flux ratio (3.11); whereas, the measured N:Ga ratio is 72% larger than the ideal 1:1 ratio (for Mn_3GaN) but only 38 % larger than the incident N:Ga flux ratio (1.25); and finally, the measured N:Mn ratio is 67% larger than the ideal 0.33 (for Mn_3GaN) but only 37 % larger than the incident N:Mn flux ratio (0.40), both indicating a N-rich surface. It is important to note that the surface composition can be influenced by the high efficiency, radio-frequency N plasma source used during the growth

TABLE III. Auger Spectroscopy Data Tabulated

Element	P-P Intensity (A.U.)	Measured Sensitivity Factor	Concentration Ratio
Mn	41030 ± 2556	1.15	-
Ga	8540 ± 1123	0.75	-
N	40865 ± 921	2.09	-
Mn:Ga	-	-	3.13 ± 0.61
N:Ga	-	-	1.72 ± 0.26
N:Mn	-	-	0.55 ± 0.05

and the precise order in which the Mn, Ga, and N fluxes were terminated. Another unknown factor is the sticking coefficient of N in comparison to that for Ga or for Mn on the Mn_3GaN surface.

2. *Oxygen Adsorption at the Surface*

We also notice an AES peak at the energy range 510-512 eV which consists of a combination of O_{510} and Mn_{512}. Using the known peak-to-peak intensity ratio (from book spectra) of Mn_{512} to Mn_{592}, we can extract the oxygen signal from the O+Mn peak complex. Details are given in Supplementary note 1. The results indicate a surface O/Mn ratio of 7.84 %, and using the results (shown in the following) for the theoretical lowest energy surface structure being Mn+Ga (1:1 ratio in the top layer), we find the surface O/(Mn+Ga) fraction = 3.92 %. Surface oxygen is most likely coming from chamber background gases, possibly from the AES filament.

G. Surface Morphology by STM

To examine the Mn_3GaN surface structure, *in-situ* STM was performed at room temperature by transferring the sample from the MBE system through a gate valve directly into the adjoining STM chamber. Fig. 7(a) shows an image of size 207 Å × 207 Å, consisting of multiple terraces separated by bilayer height steps. Terrace 4 appears to contain a threading dislocation, as suggested by the variable height step emerging out of the terrace. A line profile cutting across terraces 2, 3, and 4 is shown in Fig. 7(b). This profile shows step heights measuring 3.81 ± 0.05 Å, in good agreement with $2d = a_{Mn3GaN} = 3.863$ Å, the compressively-strained *out-of-plane* lattice constant a_l based on the weighted average of RSM, XRD, and STEM results. The 2-ML-height steps are better illustrated in the 3D perspective view shown in Fig. 7(c) and suggest that only one of the two inequivalent atomic layers is stable at the surface. Theoretical calculations (see next section) explore the question of which atomic layer is more stable - the MnGa layer or the Mn_2N layer.

There is some visible substructure within the terraces on a length scale of 1-2 nm which may indicate some surface disorder, possibly caused by nitridation, which may have occurred at the end of growth. That would be consistent with the N/Ga ratio measured by *in-situ* AES (1.72 ± 0.26) suggesting a N-rich surface and the finding (see theory section) that the Mn_2N surface is unstable.

H. Theoretical calculations

We performed first-principles calculations to study the first stages of epitaxial growth and the atomic structure at the substrate interface and at the vacuum surface of the Mn_3GaN film grown on MgO(001).

1. *High Symmetry Adsorption Sites on MgO(001) Surface*

First, to precisely understand the initial stages of growth, we have considered the adsorption of full monolayers of Mn, Ga, and N at different high symmetry sites. These sites are illustrated in Fig. 8(a). For instance, at the Top-O site, the atom is placed on the first O layer. The adsorption at Top-Mg occurs when the atom is deposited on the first Mg layer. The bridge site is reached when the atom is added between the Mg and O atoms of the first layer. For hollow sites, the atom is placed in the hollow site of the unit cell, as seen in Fig. 8(a).

Relative energies $E - E_0$ for each adsorbed atom on different high symmetry sites are calculated to determine the most stable configuration in each case, where E and E_0 are the total energy of the given configuration and the total energy of the lowest energy configuration for a given adsorbed atom, respectively. The results are listed in table IV, demonstrating that the Top-O site is the most stable configuration for all elements.

TABLE IV. Relative energies (eV) for Mn, Ga, and N adsorption at different high symmetry sites.

Site	Mn	Ga	N
Top-O	0.00	0.00	0.00
Top-Mg	2.28	0.88	9.2
Hollow	1.13	9.9	0.14
Bridge	1.87	0.68	7.8

2. *Adsorption Energies at Top-O Site*

To define the most stable configuration among Mn, Ga, and N adsorption at Top-O site, the adsorption energy was calculated (E_{ads}) from the following equation [38]:

$$E_{ads} = E_{x/MgO} - E_{MgO} - E_x \tag{8}$$

where $E_{x/MgO}$ is the total energy of the surface with the adsorption of x = Mn, Ga and N. E_{MgO} signifies the total energy of the clean MgO (001) surface, and E_x is the total energy of an isolated atom, which is modeled by placing an atom into a unit cell of 20 Å × 20 Å × 20 Å to avoid the periodic interactions. Spin-polarized calculations were employed for all elements. A negative value suggests thermo-positive and favorable adsorption.

Table V lists a summary of the adsorption energies for the Top-O site. The energies reveal that the Ga adsorption is the most stable configuration, this is partially attributed to the formation of covalent bonds. On the other hand, the N adsorption is unstable on the MgO (001) surface. Therefore, Ga adsorption was carefully considered while studying interface formation energies, and subsequently, we built different models based on Ga adsorption to explain the experimental results.

TABLE V. Adsorption energies (eV) for Mn, Ga, and N adsorption at Top-O site.

Element	E_{ads}
Mn	-2.17
Ga	-4.21
N	0.82

3. Interface Structure Optimization

The optimized structures of four different interfaces are shown in Fig. 8(b-e), and the interfacial configurations are described as follows: Fig. 8(b) represents model 1, which has a Mn_2N layer as the initial layer of Mn_3GaN and an interlayer distance at the interface of 3.39 Å. Model 2 consists of an interface between MgO and MnN, as seen in Fig. 8(c), with a bond length of 2.82 Å and 2.15 Å for N-O and Mn-O, respectively. Model 3 as shown in Fig. 8(d) consists of an interface configuration between MgO and a full Ga monolayer with a bond length of 2.78 Å. Finally, model 4 consists of an interface between MgO and MnGa, as shown in Fig. 8(e), and having an interplanar distance of 2.14 Å.

To determine the most stable interface, the interface formation energy (IFE) formalism was employed by applying the following definition [39]:

$$IFE = \frac{E_{Interface} - E_{MgO} - E_{Mn_3GaN}}{A_{interface}} + \sigma_{MgO} + \sigma_{Mn_3GaN} \tag{9}$$

where $A_{interface}$ is the interface area, $E_{interface}$ is the total energy of a fully relaxed interface structure, and where E_{MgO} and E_{Mn_3GaN} correspond to the total energy of the isolated MgO slab and isolated Mn_3GaN slab, respectively.

In Eq. (9), σ_{MgO} is the surface formation energy of the MgO surface, which is defined as:

$$\sigma_{MgO} = \frac{1}{2A}[E^{slab}_{MgO} - \frac{1}{2}(n_{Mg} + n_O)\mu^{bulk}_{MgO} - \frac{1}{2}(n_{Mg} - n_O)(\mu_{Mg} - \mu_O)] \tag{10}$$

where A is the area of the MgO surface, E^{slab}_{MgO} corresponds to the total energy of the MgO surface, and where n_i and μ_i are the number of atoms and the chemical potential of the ith species, respectively. The chemical potentials have been varied from Mg-rich conditions ($\mu_{Mg} = \mu^{bulk}_{Mg}$) to Mg-poor conditions ($\mu_{Mg} = \mu^{bulk}_{Mg}$ - $\mu^{mol}_{O_2}$). Because we have employed the ideal MgO (001) surface, i.e. no vacancies, the surface formation energy is the same for both conditions, which has a value of $\sigma_{MgO} = 0.1$ eV/[1×1 cell].

The interface formation energies of all models were computed and are displayed in Fig. 9(f) as a function of Mn and Ga chemical potentials (see the Supplementary file for 2-D graphs of this information). It is seen that both model-1 (blue) and model-2 (mauve) interfaces are unstable along all Ga and Mn chemical potentials. The MnN and Mn_2N interfaces are unstable due to the formation of covalent bonds between N and O, as discussed in the adsorption study. Model-3 (green), consisting of a Ga atomic layer, represents the most stable interface under Ga-rich conditions for the whole range of Mn chemical potential. Nonetheless, Ga-rich conditions were most likely not reached in the experiment. On the other hand, model-4 (red), consisting of a MnGa atomic layer, is stable for Ga-poor conditions for both Mn-rich and Mn-poor conditions. This is consistent with the experimental conditions.

We can conclude that the most favorable interface under the observed experimental (Mn-rich) conditions is formed by MnGa on MgO. This result differs from the previous work by Quintela *et al.*[6] who found a stable interface between Mn_2N and AlO_2. Both results reveal the important role played by the substrate in determining the film/ substrate interface.

4. *Lowest Energy Surface Model*

The surface formation energy of the Mn_3GaN surface is represented by σ_{Mn_3GaN}, and since Mn_3GaN is a ternary compound, and since the Mn and Ga fluxes were regulated by experimental conditions, the surface formation energy can be written in the following form, as has been applied in other ternary systems [40–42]:

$$\sigma_{Mn_3GaN} = \phi - \frac{1}{A}[(n_{Mn} - 3n_N)\Delta\mu_{Mn} - (n_{Ga} - n_N)\Delta\mu_{Ga}] \tag{11}$$

with

$$\phi = \frac{1}{A}[E^{slab}_{Mn_3GaN} - n_N E^{bulk}_{Mn_3GaN} - (n_{Mn} - 3n_N)E^{bulk}_{Mn} - (n_{Ga} - n_N)E^{bulk}_{Ga}] \tag{12}$$

where $E^{slab}_{Mn_3GaN}$ is the total energy of each Mn_3GaN slab, $E^{bulk}_{Mn_3GaN}$ is the total energy of Mn_3GaN in bulk, E^{bulk}_{i} is the total energy of Mn and Ga in bulk, and $\Delta\mu_{Mn}$ and $\Delta\mu_{Ga}$ are the variations of the Mn and Ga chemical potentials, respectively.

The E^{bulk}_{Mn}, E^{bulk}_{Ga}, $E^{mol}_{N_2}$ and $E^{bulk}_{Mn_3GaN}$ energies have been calculated by modeling a) the α-Mn bulk phase with 58 atoms per unit cell; b) the Ga bulk phase in its normal crystalline unit cell; c) the isolated N_2 molecule in a cube of 20 Å × 20 Å × 20 Å; and d) the ternary Mn_3GaN alloy in its antiperovskite structure unit cell. In a similar way, the chemical potentials μ_{Mg} and μ_{O_2} have been obtained by modeling Mg in its hexagonal unit cell and O_2 with an isolated O_2 molecule in a cube of 20 Å × 20 Å × 20 Å.

Regarding the variations of the chemical potentials, the individual chemical potential of each atomic species (Mn, Ga, N) must be less than the corresponding values for the pure bulk of the same atomic species. Otherwise, these atoms would precipitate into their elemental forms out of the Mn_3GaN material. Therefore, the upper boundary conditions for the variations of the chemical potentials can be written as:

$$\Delta\mu_{Mn} = \mu_{Mn} - E^{bulk}_{Mn} < 0 \tag{13}$$

$$\Delta\mu_{Ga} = \mu_{Ga} - E^{bulk}_{Ga} < 0 \tag{14}$$

$$\Delta\mu_{N} = \mu_{N} - \frac{E^{mol}_{N_2}}{2} < 0 \tag{15}$$

Furthermore, the total energies of the elements and their ternary alloy in their ground states are related to the enthalpy of formation of Mn_3GaN by the formula:

$$-\Delta H^{f}_{Mn_3GaN} = E^{bulk}_{Mn_3GaN} - 3E^{bulk}_{Mn} - E^{bulk}_{Ga} - E^{mol}_{N_2}. \tag{16}$$

with a computed value of $\Delta H^{f}_{Mn_3GaN}$ = -1.58 eV. The lower boundary conditions are obtained combining equations (13), (14), (15) and the energy-chemical potential relationship:

$$E^{bulk}_{Mn_3GaN} = 3\mu_{Mn} + \mu_{Ga} + \mu_{N} \tag{17}$$

resulting in the formula:

$$3\Delta\mu_{Mn} + \Delta\mu_{Ga} > \Delta H^{f}_{Mn_3GaN} \tag{18}$$

Considering the previous equations, $\Delta\mu_{Mn}$ has the following limits: Mn-rich conditions ($\Delta\mu_{Mn} = 0$) and Mn-poor conditions ($\Delta\mu_{Mn} = \Delta H^f_{Mn_3GaN}/3$). Similarly, the limits for $\Delta\mu_{Ga}$ are: Ga-rich conditions ($\Delta\mu_{Ga}$=0) and Ga-poor conditions ($\Delta\mu_{Ga} = \Delta H^f_{Mn_3GaN}$).

5. *Surface Formation Energy Plots*

Therefore, we have calculated and plotted the surface formation energies of isolated Mn_3GaN surfaces of the 4 models from Mn-poor to Mn-rich conditions, as well as from Ga-poor to Ga-rich conditions (see Supplementary file for a plot of the surface formation energies in 2-D). A top view of the isolated surfaces of each model is illustrated in Fig. 9(a-d). Figure. S3 depicts a side view of the atomic schemes for the isolated surfaces. As seen in Fig. 9(e), model-1 (blue) and model-2 (mauve) are Mn_2N and MnN surface models and are the least favorable configurations in all Mn and Ga chemical potentials. Model-3 (green) consists of a full Ga monolayer and is the most stable surface at Ga-rich conditions including for the whole range of Mn chemical potential. However, since Ga-rich conditions were not likely reached in the experiment, it suggests model-4 (red), consisting of a MnGa monolayer, as the most likely observed surface structure. This configuration is the most stable surface under Ga-poor conditions for both Mn-poor and Mn-rich conditions.

TABLE VI. Interlayer distances (Å) of different layers for Model-4.

Interlayer distances	Mn-N	Mn-Ga
d_{1-2}	1.90	1.78
d_{2-3}	1.89	1.81
d_{3-4}	1.87	1.85
d_{4-5}	1.87	1.88
d_{5-6}	1.89	1.78
d_{6-7}	1.87	1.67

We also investigated the structural properties of the Mn_3GaN (001) surface of model-4. As seen in Fig. 8(e), two types of interlayer distances can be distinguished: one between Mn and N (Mn-N), and another between Mn and Ga (Mn-Ga). Table VI gives interlayer distances between consecutive layers going into the bulk. Although every interlayer distance is possible from this data, based upon the fact that the MnN-terminated surfaces are energetically unfavorable, we should expect to only find bi-layer (from 3.74 Å to 3.79 Å) step heights, in agreement with the STM step height profile measurement presented in Fig. 7(b).

I. Discussion

Although theory predicts a MnGa lowest energy surface, the AES measurements found a N/Ga ratio of 1.72. This suggests possible disagreement with experiment. However, we must first consider that the N:Ga flux ratio itself was set at 1.25:1, which itself could lead to surface with excess nitrogen. Furthermore, as noted before, the amount of N present at the surface might be affected by the precise sequence of shutdown of the N, Ga, and Mn fluxes at the growth termination. Only a 1/2 second delay on closing the N source could lead to an excess of 1.5-2.0 $\times$ 10^{14} N atoms/cm^2 compared to one monolayer = 6.47 $\times$ 10^{14} Ga/cm^2 (defined as 1 Ga/(3.932 $\times$ 10^{-8} cm)^2), thus adding an additional 0.23 ML of nitrogen. Together this could give easily 1/2 ML of excess N, potentially explaining the measured AES N:Ga ratio (1.72 ± 0.26).

IV. SUMMARY

We have presented experimental and theoretical results for the surface, film, and interface properties of crystalline thin films consisting of Mn_3GaN epitaxially grown on cubic MgO (001) substrates. RHEED shows that the film grows smoothly, consistent with *in-situ* STM measurements which reveal atomically-smooth terraces separated by 2 ML height step edges, consistent with bi-layer height steps. Careful analysis of the RHEED patterns show that after only 25 min of growth, the lattice has evolved towards a close-to bulk value for Mn_3GaN but retaining both *in-plane* and *out-of-plane* strain. Chemical stoichiometry measurements by *in-situ* AES and *ex-situ* EDS (STEM) are consistent with a 3:1:1 compound ratio, and AES ratios suggest a slightly N-rich surface, consistent with the growth conditions. Measurements of the film lattice constants reveal a small amount of remnant strain originating most likely from the lattice mismatch with the MgO substrate. The *in-plane* (transverse) strain ϵ_t is determined to be +0.31 ± 0.34 %, while the *out-of-plane* (longitudinal) strain ϵ_l is found to be -1.22 ± 0.13 %, corresponding to a derived lattice constant for a relaxed film of 3.922 ±

0.011 Å and a Poisson's ratio of 0.260 (theoretical value).

Non-collinear first-principles calculations were employed to investigate the structural properties at the surface and interface. The adsorption study showed that all chemical species (Mn, Ga, and N) prefer to bond with O atoms, making Ga and Mn adsorption favorable. According to the surface and interface formation energies, Model-4 (MnGa) is the most stable configuration under Mn-rich/Ga-poor conditions. Model-1 and Model-2 lose stability due to unstable bonds between N and O, as presented in the adsorption study. Model-3 (Ga layer) should become stable under Ga-rich conditions. Therefore, for the experimental conditions shown in this work, the interface is expected to consist of MnGa/MgO with a MnGa-terminated surface. We note that if the surface were consisting of a Mn_2N final termination, we could expect a much larger N:Ga ratio in AES (since there would be no Ga at the surface). Therefore, the AES result, although suggesting a slightly N-rich surface is consistent with a stable MnGa surface termination. This study opens the door to future more detailed investigations of the structural, magnetic, and electronic properties of antiperovskite Mn_3GaN surfaces and thin films of interest for antiferromagnetic spintronics.

ACKNOWLEDGMENTS

This research has been supported by the U.S. Department of Energy, Office of Basic Energy Sciences, Division of Materials Sciences and Engineering under Award No. DE-FG02-06ER46317 (MBE, RHEED, AES, STM, and XRD studies) and Award No. DE-SC0001304 (RSM studies). J.C. Moreno thanks CONACYT for his doctoral scholarship. Calculations were performed in the Laboratorio Nacional de Supercómputo del Sureste de Mexico. STEM measurements were performed at the Michigan Center for Materials Characterization. The authors would also like to thank Professor Eric Stinaff (Ohio University) and his Ph.D. student William Poston for titanium back-coating of substrates. The authors also acknowledge WSxM software for STM image processing [43].

DATA AVAILABILITY

The data supporting this study's findings are openly available in Zenodo at [Link will be added later].

[1] S. Upadhyay, T. Erickson, H. Hall, A. Shrestha, D. C. Ingram, K. Sun, A. R. Smith, J. Vac. Sci. Technol. A, **41(4)** (2023).

[2] S. Upadhyay, T. Erickson, H. Hall, A. Shrestha, D. C. Ingram, K. Sun, A. R. Smith, Surfaces and Interfaces, **42**, 103379 (2023).

[3] D. J. Lin, B. C. Lim, Y. Y. K. Hnin, N. C. Lim, H. Y. Lee, H. K. Tan, P. Ho, Journal of Electronic Materials, 1-7 (2023).

[4] J. T. Holguín-Momaca, C. J. Muñoz-Carnero, H. Sharma, C. R. Santillán-Rodríguez, J. A. Matutes-Aquino, C. V. Tomy, S. F. Olive-Méndez, Journal of Magnetism and Magnetic Materials, **471**, 329-333 (2019).

[5] E. F. Bertaut, D. Fruchart, J. P. Bouchaud, and R. Fruchart, Solid State Commun, **6**, 251 (1968).

[6] C. X. Quintela, K. Song, D. F. Shao, L. Xie, T. Nan, T. R. Paudel, C. B. EOM, Science Advances, **6(30)**, eaba4017 (2020).

[7] M. E. Fruchart, M. R. Fruchart, Solid State Communications, **8(1)**, 49-51 (1970).

[8] J. P. Bouchaud, R. Fruchart, R. Pauthenet, M. Guillot, H. Bartholin, F. Chaissé, Journal of Applied Physics, **37(3)**, 971-972 (1966).

[9] P. L'Heritier, D. Boursier, R. Fruchart, D. Fruchart, Materials Research Bulletin, **14(9)**, 1203-1212 (1979).

[10] Y. You, H. Bai, X. Feng, X. Fan, L. Han, X. Zhou, C. Song, Nature Communications, **12(1)**, 6524 (2021).

[11] D. Matsunami, A. Fujita, K. Takenaka, M. Kano, Nature Materials, **14(1)**, 73–78 (2015).

[12] S. V. Krivovichev, Zeitschrift für Kristallographie-Crystalline Materials, **223**, 109–113 (2008).

[13] P. Lukashev, R. F. Sabirianov, Journal of Applied Physics, **107(9)**, (2010).

[14] G. Gurung, D. F. Shao, T.R. Paudel, E. Y. Tsymbal, Phys. Rev. Mat, **3(4)**, 044409 (2019).

[15] K.H. Kim, K. J. Lee, H. S. Kang, F.C. Yu, J. A. Kim, D. J. Kim, Y. E. Ihm, phys. stat. sol. (b), **241(7)**, 1458-1461 (2004).

[16] K. H. Lee, K. H. Kim, F. C. Yu, W. S. Im, C. X. Gao, D. J. Kim, H. J. Kim, Y. E. Ihm, phys. stat. sol. (b), **241(12)**, 2854-2857 (2004).

[17] P. Lukashev, R. F. Sabirianov, K. Belashchenko, Physical Review B, **78(18)**, 184414 (2008).

[18] S. Ishino, J. So, H. Goto, T. Hajiri, H. Asano, AIP Advances, **8(5)** (2018).

[19] T. Nan, C. X. Quintela, J. Irwin, G. Gurung, D. F. Shao, J. Gibbons, C. B. Eom, Nature communications, **11(1)**, 4671 (2020).

[20] B. H. Rimmler, B. K. Hazra, B. Pal, K. Mohseni, J. M. Taylor, A. Bedoya-Pinto, S. S. Parkin, Advanced Materials, **35(23)**, 2209616 (2023).

[21] G. Kresse, J. Furthmuller, Phys. Rev. B. **54**, 11169 (1996).

[22] G. Kresse, J. Furthmuller, Phys. Rev. B. **54**, 11169 (1996).

[23] B. H. Hammer, L. B. Hansen, J. K. Nørskov, Phys. rev. B, **59**, 7413 (1999).

[24] H. J. Monkhorst, J. D. Pack, Phys. rev. B, **13**, 5188 (1976).

[25] C. Su, J. Zhang, Computational Materials Science, **189**, 110257 (2021).

[26] B. Sarpi, R. Daineche, C. Girardeaux, A. Hémeryck, S. Vizzini, Appl. Surf. Sci., **361**, 259-264 (2016).

[27] S. Hasegawa, Characterization of Materials, **97**, 1925-1938 (2012).

[28] A. Foley, J. Corbett, A. L. Richard, K. Alam, D. C. Ingram, A. R. Smith, Journal of Crystal Growth, **446**, 60-67 (2016).

[29] A. Shrestha, J. C. M. Hernandez, A. Abbas, G. H. Cocoletzi, N. Takeuchi, D. C. Ingram, A. R. Smith, Applied Surface Science, **664**, 160152 (2024).

[30] J. M. Van Hove, P. Pukite, P. I. Cohen, C. S. Lent, Journal of Vacuum Science Technology A: Vacuum, Surfaces, and Films, **1(2)**, 609-613 (1983).

[31] H. Yang, H. Al – Birthen, E. Trifan, D . C. Ingram, and A. R. Smith, J. Appl. Phys. 91, 3 (2002.

[32] S. Ishino, J. So, H. Goto, T. Hajiri and H. Asano, AIP Advances,**8(5)**(2018).

[33] Scherrer, P. J. M. P. (1918). Nachr Ges wiss goettingen. Math. Phys., 2, 98-100.

[34] U. Holzwarth, N. Gibson, Nature Nanotech 6, 534 (2011). https://doi.org/10.1038/nnano.2011.145

[35] B. Wang, M. Zhang, V. Adhikari, P. Fang, S. V. Khare, D. Gall, Journal of Materials Chemistry C, **8(36)**, 12677-12688 (2020).

[36] Images and video generated using CrystalMaker®: CrystalMaker Software Ltd, Oxford, England, see www.crystalmaker.com.

[37] A. Azouaoui, N. Benzakour, A. Hourmatallah, K. Bouslykhane, Philosophical Magazine, **101(13)**, 1587-1601 (2021).

[38] Y. Zhou, H. Xiong, Y. Yin, S. Zhong, RSC advances, **9**, 1752-1758 (2019).

[39] K. Alam, R. Ponce-Pérez, K. Sun, A. Foley, N. Takeuchi, A. R. Smith, J. Vac. Sci. Technol. A, **41** (2023).

[40] F. Bottin, F. Finocchi, C. Noguera, Phys. Rev. B, **68**, 035418 (2003).

[41] Zhang, H. Z., and Wang, S. Q. Acta Materialia, **55**, 4645-4655 (2007).

[42] V. Ríos-Vargas, R. Ponce-Pérez, M. G. Moreno-Armenta, J. Guerrero-Sánchez, J. Phys. D: Appl. Phys., **55**, 485003 (2022).

[43] I. Horcas, R. Fernandez, J. M. Gomez-Rodriguez, J. Colchero, J. Gomez-Herrero, and A. M. Baro, Rev. Sci. Instrum, **78**, 013705 (2007).

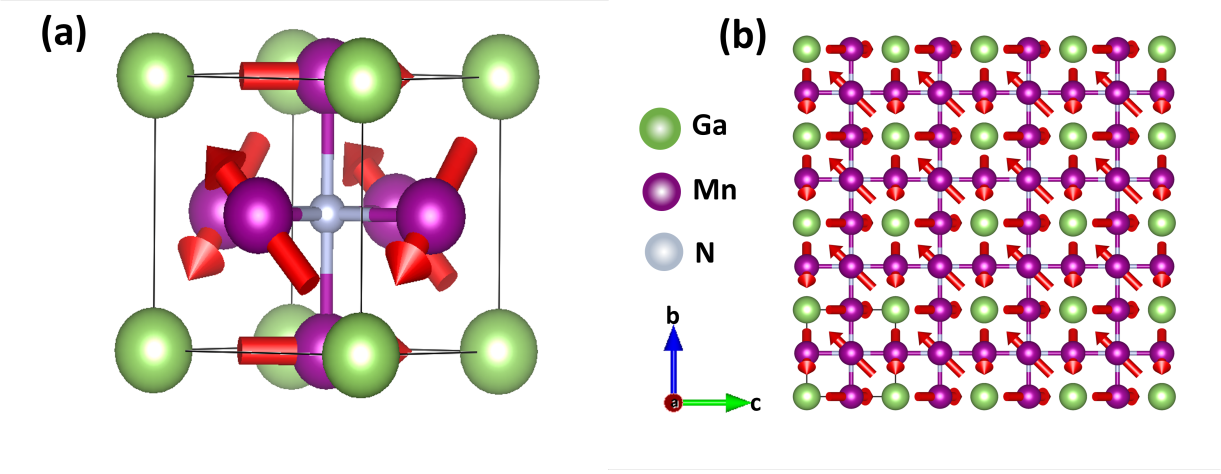

FIG. 1. (a) Schematic representation of cubic antiperovskite structure showing spin vectors in 3D perspective view; (b) view of atomic and spin structure along [001] showing 2 atomic layers.

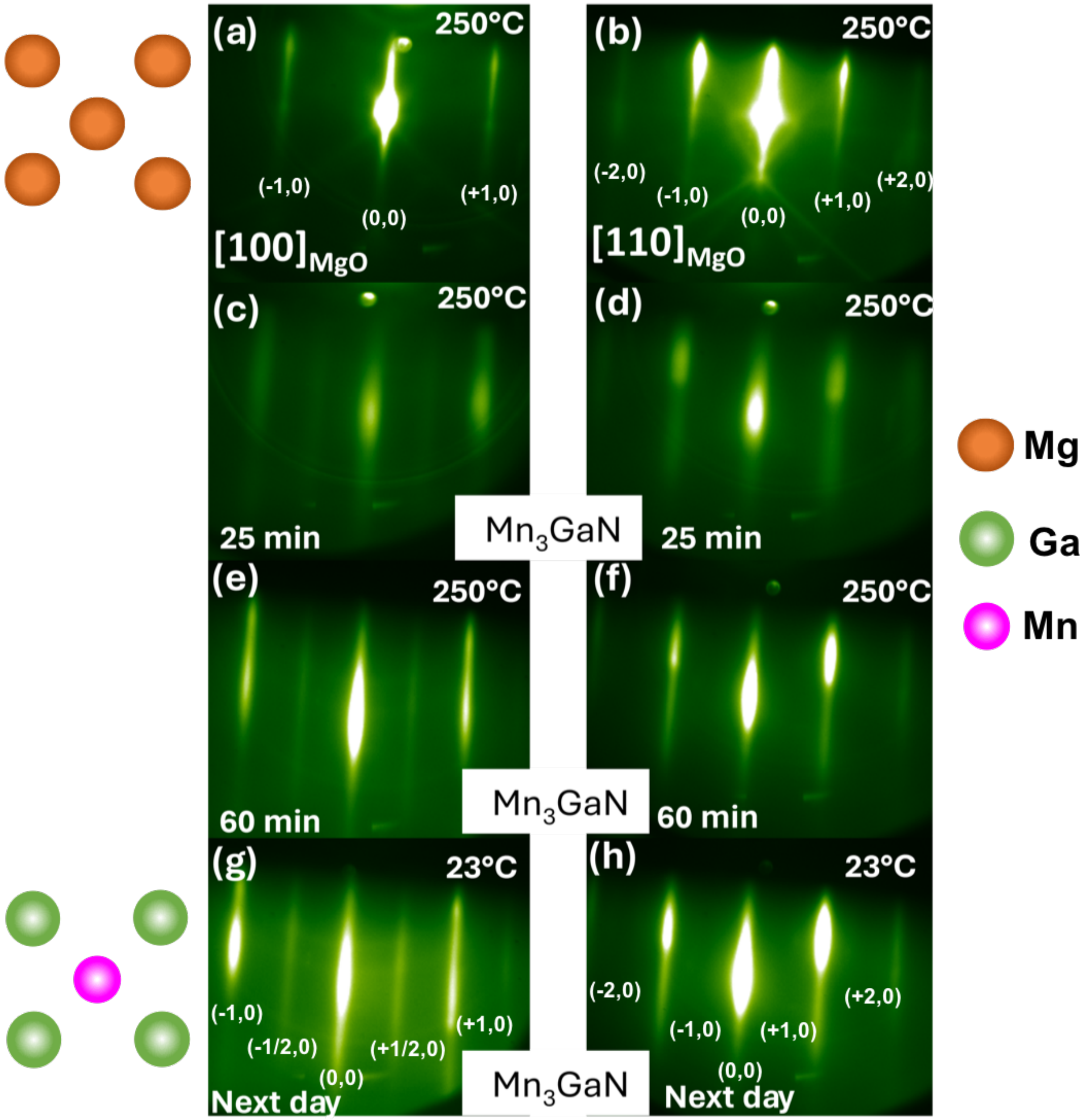

FIG. 2. Evolution of RHEED pattern during sample growth: (a) & (b) MgO substrate at 250 °C; (c) & (d) Mn_3GaN after 25 minutes of growth; (e) & (f) Mn_3GaN after 60 minutes; (g) & (h) Mn_3GaN, next day at 23°C.

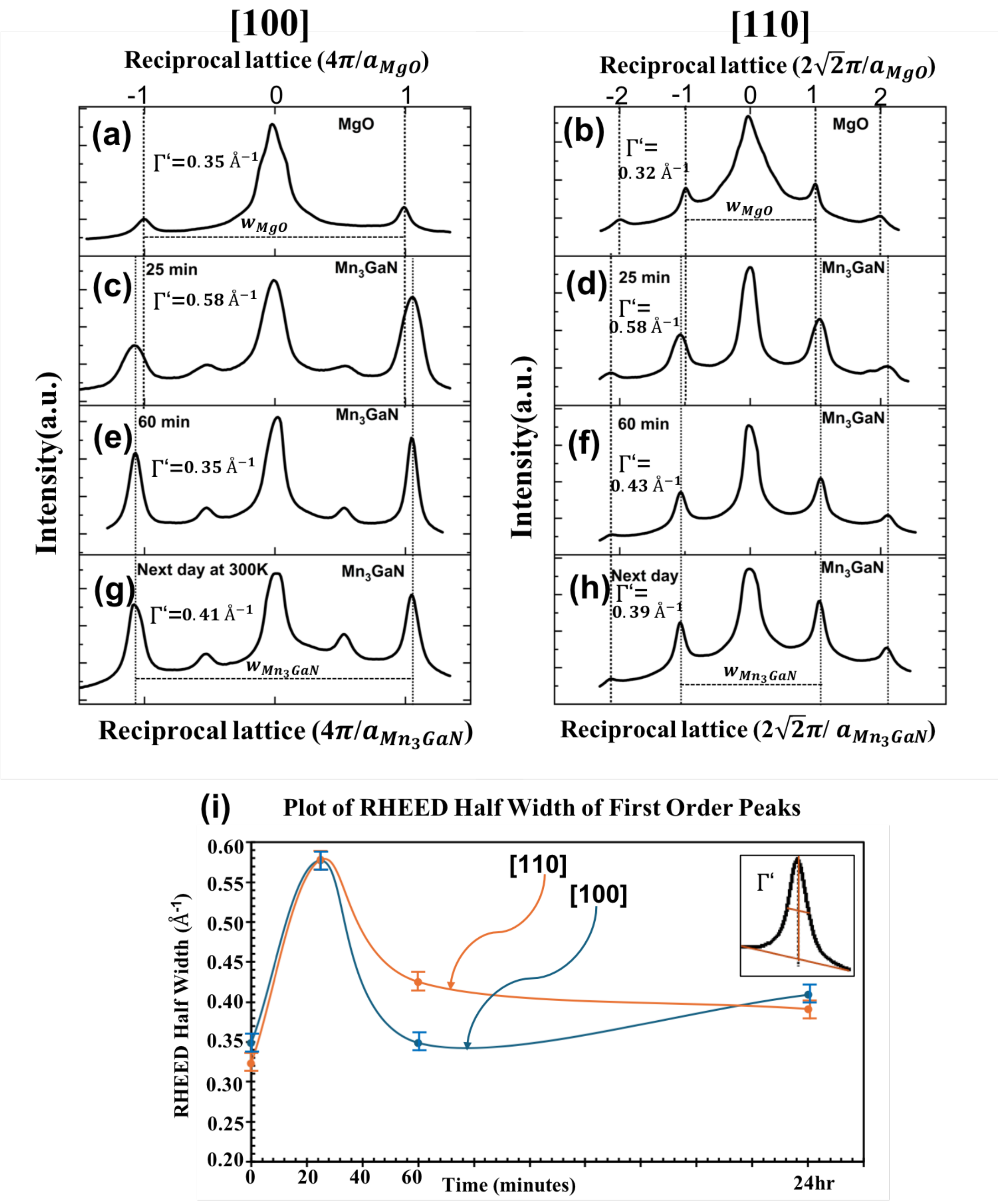

FIG. 3. Line profile of $\mathrm{Mn_3GaN}$ RHEED pattern in Fig. 2 along $[100]_{MgO}$ and $[110]_{MgO}$ directions: (a) & (b) MgO substrate before growth; (c) & (d) $\mathrm{Mn_3GaN}$ line profile after 25 minutes of growth; (e) & (f) $\mathrm{Mn_3GaN}$ line profile after 60 minutes; (g) & (h) $\mathrm{Mn_3GaN}$ line profile next day, at 23°C; (i) RHEED Half Width of first order $\mathrm{Mn_3GaN}$ peaks along $[100]_{MgO}$ and $[110]_{MgO}$.

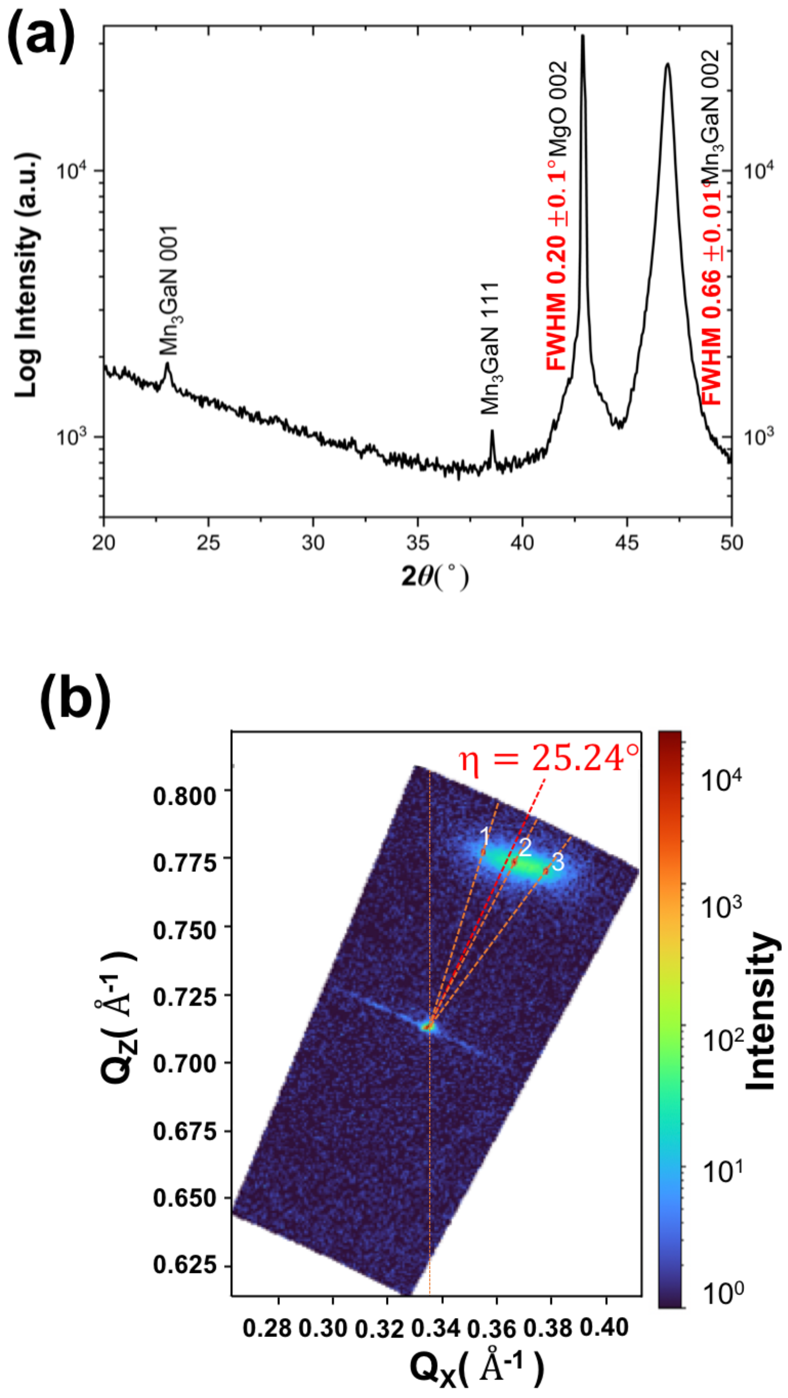

FIG. 4. (a) XRD pattern of Mn_3GaN (001) grown on MgO (001) substrate at 250 °C. The pattern reveals different peaks on the log scale. (b) Asymmetric (103) RSM scan of strain relaxed Mn_3GaN thin film.

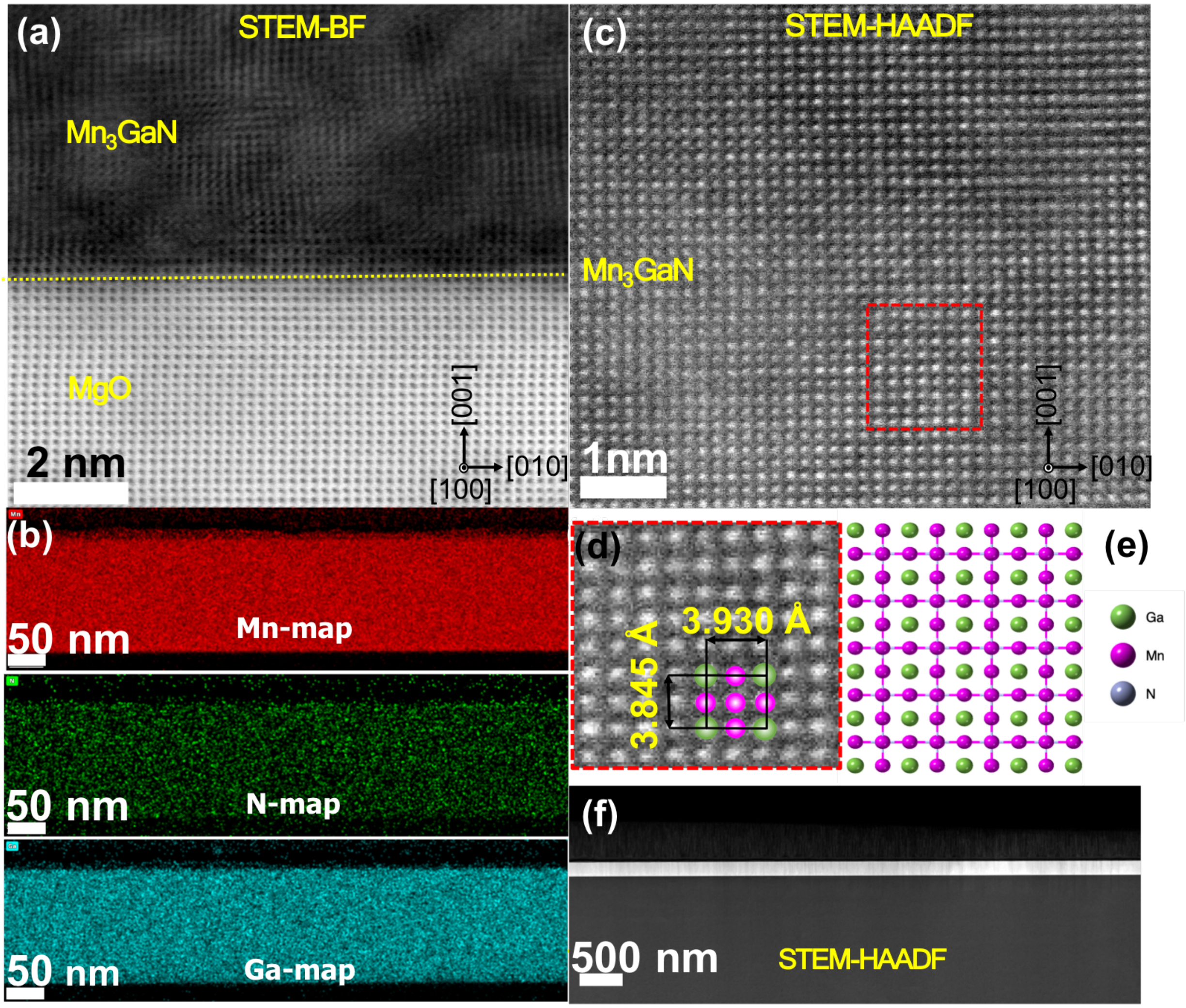

FIG. 5. (a) Bright-field image of the interface between MgO and grown Mn_3GaN; (b) Elemental analysis showing the composition of Mn, N, and Ga for the sample; (c)(d) High-resolution lattice image of Mn_3GaN showing Mn and Ga atomic sites; (e) *a*-plane crystal model showing the Ga and Mn atoms with green and purple atoms; (f) 500 nm STEM-HAADF image showing flat and epitaxial film.

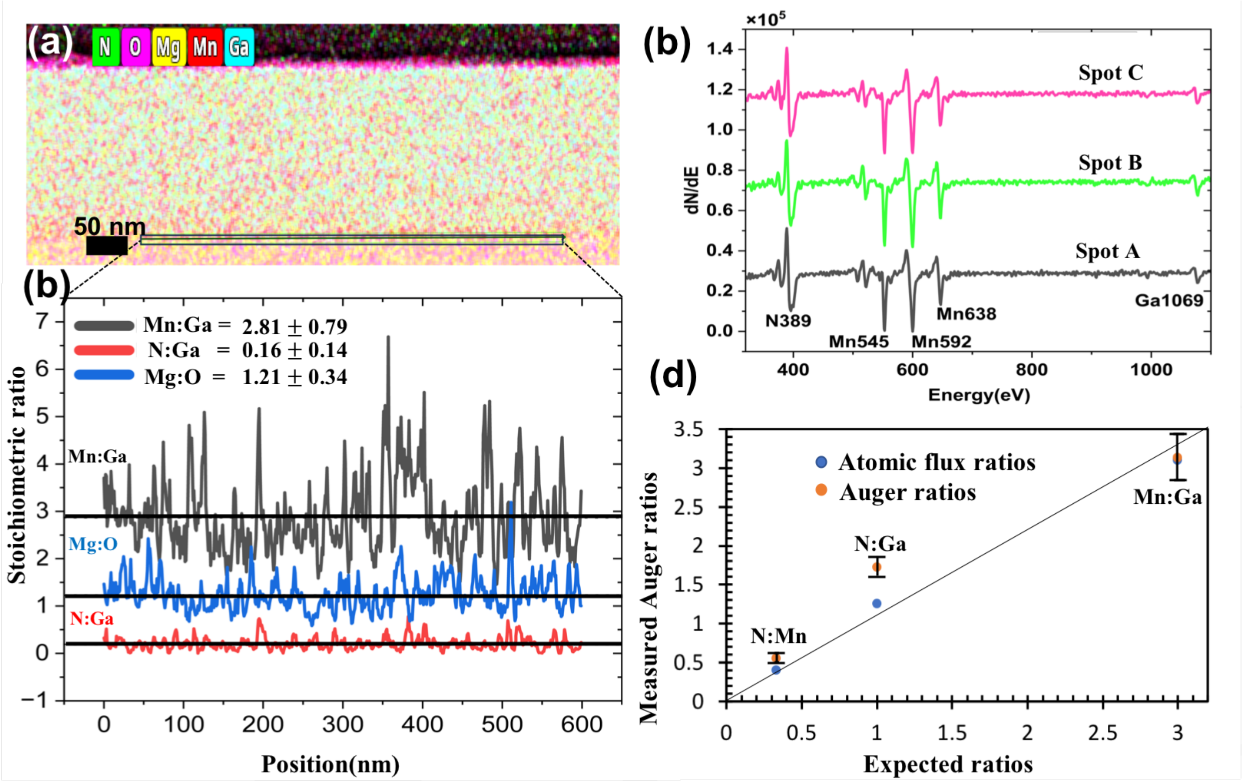

FIG. 6. (a) EDS elemental mapping of the grown Mn_3GaN film; (b) line profiles along the film/substrate interface in (a); (c) AES spectra showing the manganese, gallium, and nitrogen peaks of the Mn_3GaN sample. Spectra were taken at three different positions, as indicated by dark grey, light green, and magenta lines; (d) Graph showing measured auger ratios and atomic flux ratios of Mn:Ga, N:Ga and N:Mn.

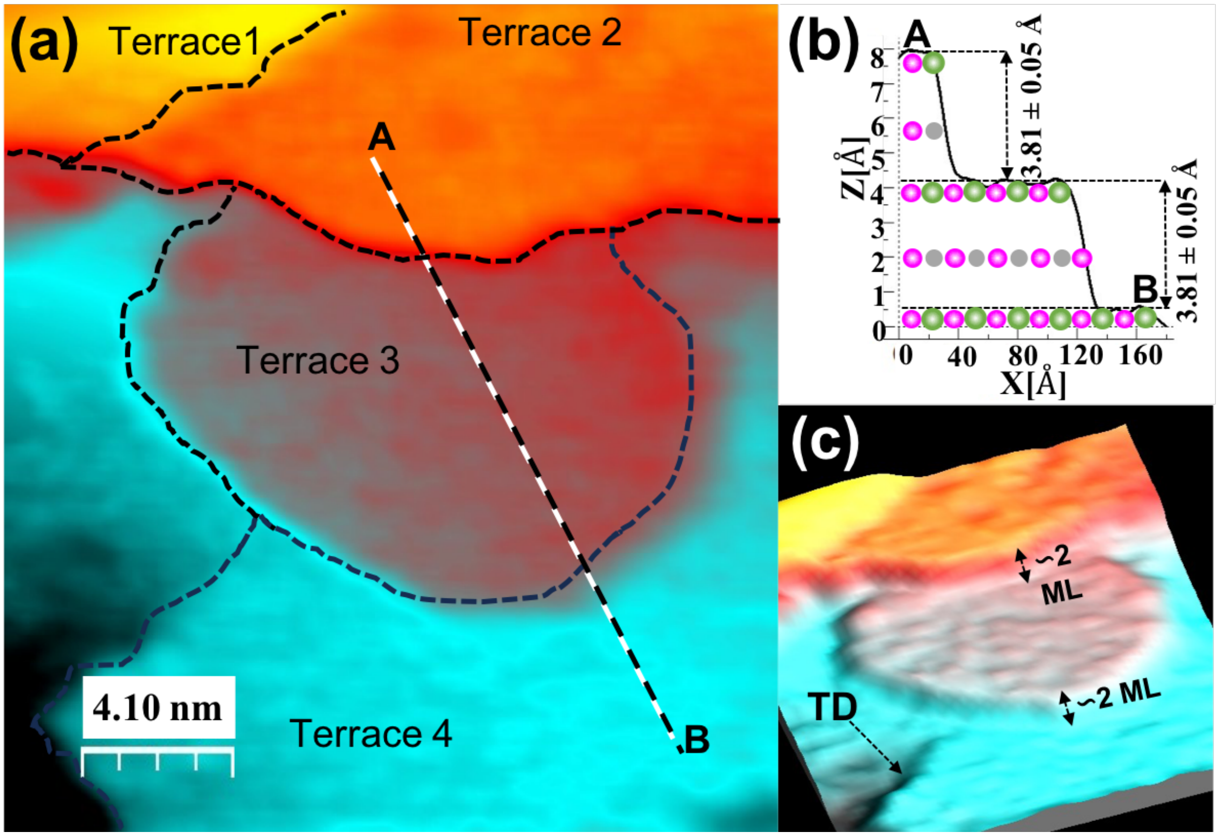

FIG. 7. STM image of Mn_3GaN grown on MgO(001). Scanning parameters; V_{bias} = 1.50 V and I_s = 69 pA. (a) 17.2 nm × 22.1 nm topographic (constant current) image showing multiple terraces. Terrace edges are highlighted by black dashed lines; (b) and (c) show the corresponding line profile along AB and a 3-dimensional perspective view of the topographic image shown in (a), respectively.

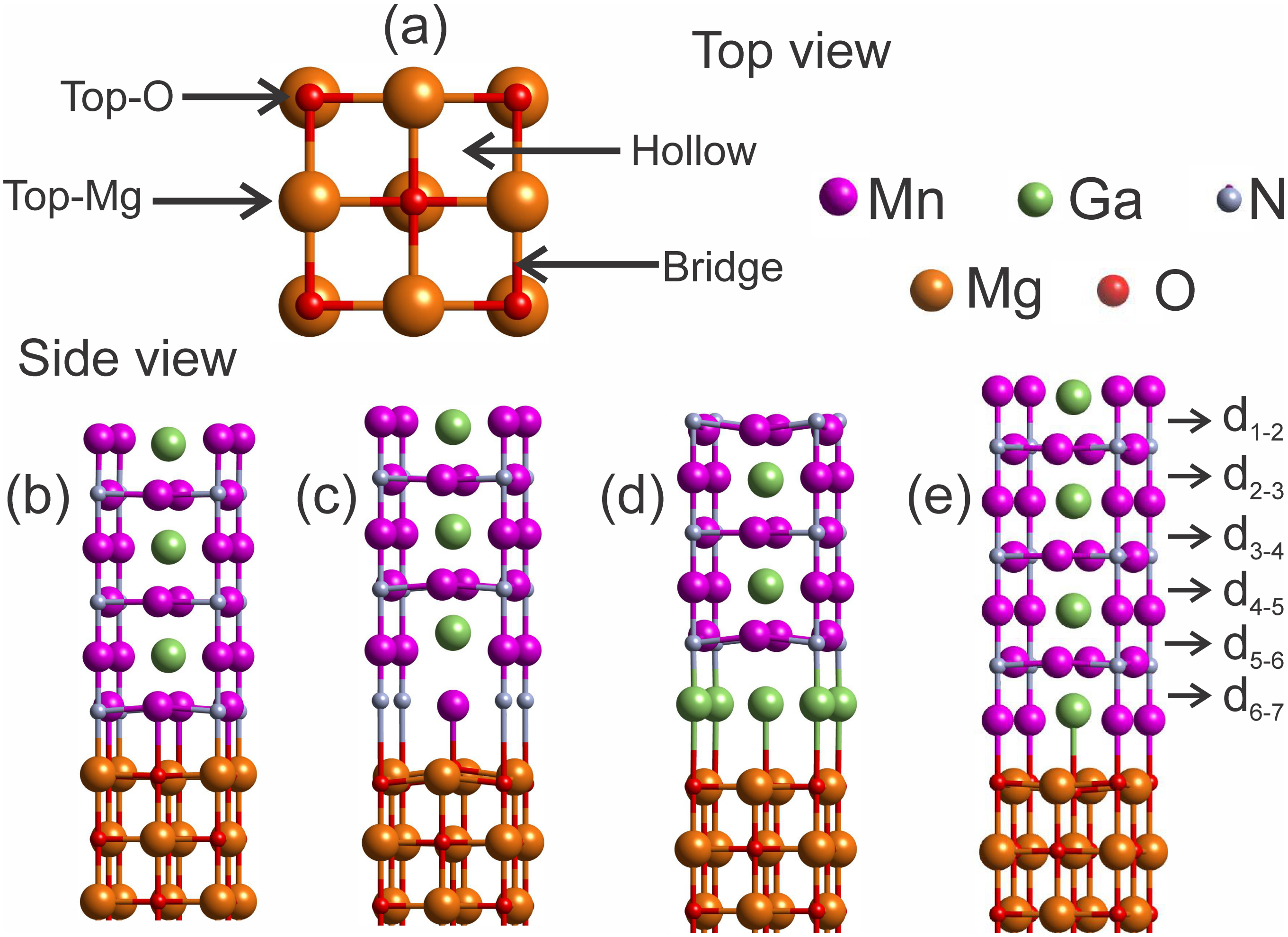

FIG. 8. (a) Top view of high symmetry sites for (001) MgO surface; (b-e) side views of the different interfaces models 1-4.

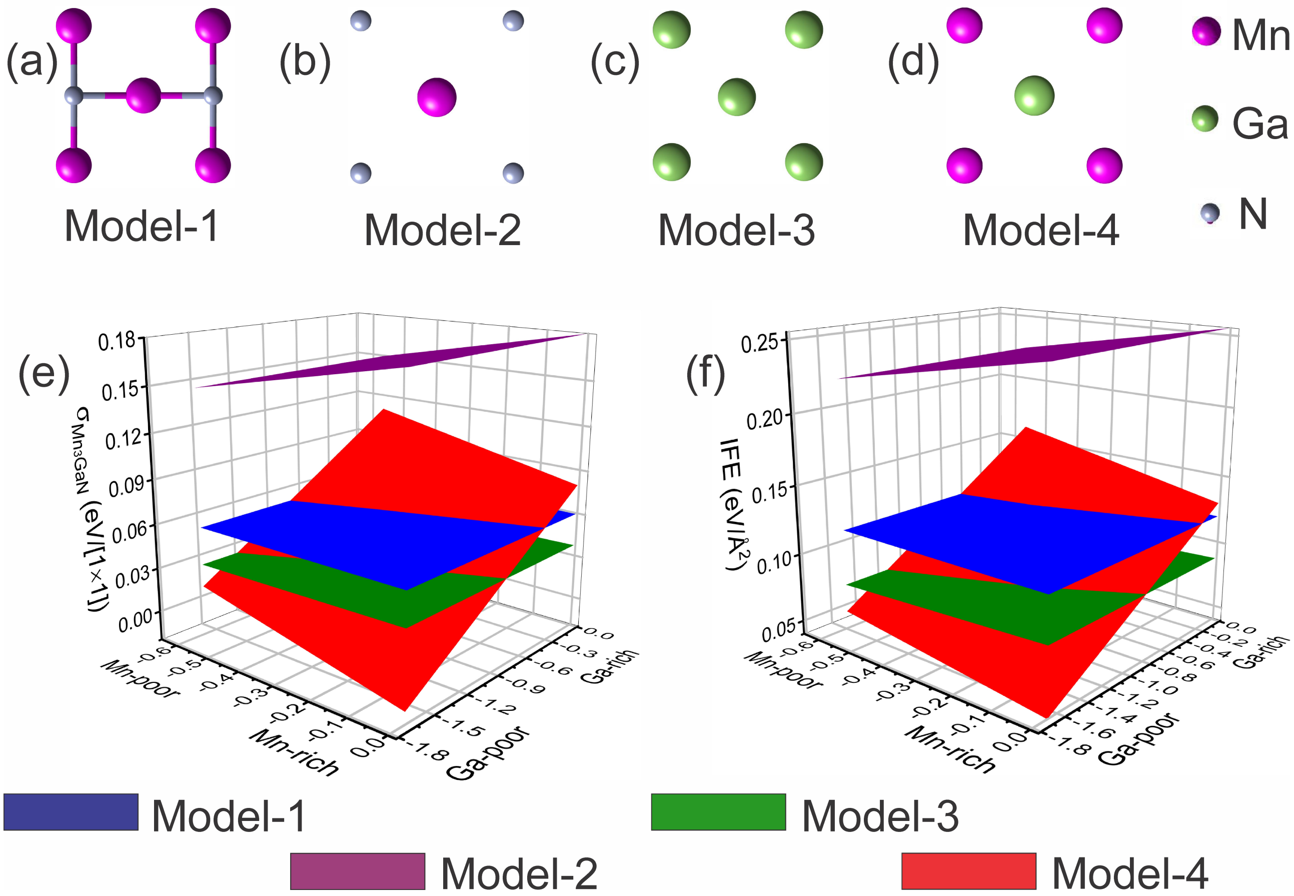

FIG. 9. (a)-(d) Top view of the isolated surfaces for models 1-4, respectively; (e) 3-D surface plot of the surface formation energies for the isolated surfaces of the four models; (f) 3-D surface plot of the interface formation energies for the different interface models.